Novel Concepts for Improved Nonlinear Transmission Line Performance

Hui Shi, W.-M. Zhang, C. W. Domier, N. C. Luhmann, Jr., L. B. Sjogren, and H.-X. L. Liu

Abstract—**Three new device concepts have been investigated to improve the performance of nonlinear transmission lines (NLTL's). These devices, the Multi-Quantum Barrier Varactor, the Schottky Quantum Barrier Varactor, and the Schottky Superlattice Quantum Barrier Varactor, are predicted to offer significant advantages over the conventional Schottky varactor because of their stronger C–V nonlinearities, symmetric C–V characteristics, high cutoff frequency and increased breakdown voltages. The wave evolution on an NLTL has been numerically investigated using an improved model in which the effects of skin losses, line parasitics and device leakage current have been included. Combining a new transmission line layout design, which permits one to double and even triple the voltage handling capability of the NLTL (dependent upon the minimum pulse duration requirements), with a back-to-back device configuration, enables both positive and negative voltage waveforms to be efficiently compressed. These new devices are shown to be useful in high power harmonic generation applications as well.**

I. Introduction

With a Schottky diode varactor [1]–[3] as the nonlinear element, pulses with durations[1] of a few picoseconds and shock waves with rise times of sub-picoseconds have been generated using NLTL's. Harmonic generation on NLTL's has also been studied [4]–[6]. However, there are several limitations for the varactors currently employed on NLTL's. First, the breakdown characteristics of GaAs Schottky varactors have limited the magnitude of picosecond solitons and shock waves. The best experimental result reported on impulse compression so far is 12.1 V peak voltage and 4.9 ps pulse duration [7]. Second, due to the small $C_{\max}/C_{\min}$ ratio of Schottky varactors, the nonlinearity is not sufficiently strong to efficiently compress the wave. Here, $C_{\max}$ and $C_{\min}$ are the maximum and minimum capacitances, respectively, of the device over the range of applied voltages. As a result, a longer line is required to compress the wave and additional losses are introduced. Efforts have been made to improve the $C_{\max}/C_{\min}$ ratio by doping the Schottky varactor hyperabruptly [8]. However, as a trade off, the signal amplitudes are further limited. Third, due to a large $C_{\min}$ value per unit area, the Schottky varactor has limited cutoff frequency. Although the final pulse width on an NLTL is determined by the Bragg frequency (a cutoff frequency arising from the periodic structure of the NLTL), generation of pulses on NLTL's requires that the Bragg frequency be several times smaller than the varactor cutoff frequency. Otherwise, a shock wave will result. Ultimately, therefore, the minimum pulse width which may be generated on an NLTL is limited by the varactor cutoff frequency and the total line loss. In addition, the Schottky diode only functions as a varactor under reverse bias, which further restricts the performance of NLTL's.

In this paper, we report on studies of NLTL's utilizing three new devices: the Multi-Quantum Barrier Varactor (MQBV) [9], the Schottky Quantum Barrier Varactor (SQBV) [9] and the Schottky Superlattice Quantum Barrier Varactor (SSQBV) [10].[2] In Section II, we discuss characteristics of the new devices and point out their advantages over conventional Schottky varactors. Circuit models for these new devices are presented in Section II together with a model for an NLTL employing these devices. In Section III, we show the results of simulations that demonstrate the effects of the special characteristics of these new devices, such as the symmetric C–V curve. This is followed by simulation results concerning pulse formation and harmonic generation employing these new devices. Effects of the leakage current associated with quantum barrier devices are discussed in this section as well. In the above studies, experimentally measured device characteristics are utilized. Finally, solutions to the leakage current problem are discussed in Section IV.

II. Simulation Model

A. Device Characteristics and Their Circuit Models

The MQBV is a stacked $Al_xGa_{1-x}As/GaAs$ quantum barrier varactor [9], with a barrier height of about 0.3 eV. Fig. 1(a) shows the epitaxial profile of an MQBV and the corresponding equivalent circuit, where r_s is the series resistance and r_d is the leakage resistance.

Since there is no zero-bias depletion layer due to the flat-band approximation, the value of $C_{\max}$ per unit area of a single barrier is approximately ϵ/W_b, where W_b is the barrier width.[3] The $C_{\max}$ value per unit area of Schottky varactor

Manuscript received February 22, 1993; revised July 13, 1994. This work was supported by the U.S. Army Research Office, the California MICRO program, Northrop Corp., the U.S. Department of Energy, and the Joint Services Electronics Program.

H. Shi, W.-M. Zhang, C. W. Domier, and N. C. Luhmann, Jr. are with the Department of Electrical Engineering, University of California Los Angeles, Los Angeles, CA 90024 USA.

L. B. Sjogren is with the TRW Electronic Technology Division, Redondo Beach, CA 90278 USA.

H.-X. L. Liu is with Loral Space Systems, Palo Alto, CA 94303 USA.

IEEE Log Number 9408561.

[1] In this paper, we define the width at half amplitude as the pulse width or duration.

[2] Note that the superlattice barrier varactor described in [10] does not include the Schottky barrier

[3] Note that $W_b = 200$ Å and there is no 50 Å undoped region next to both sides of the barrier as shown in Fig. 1.

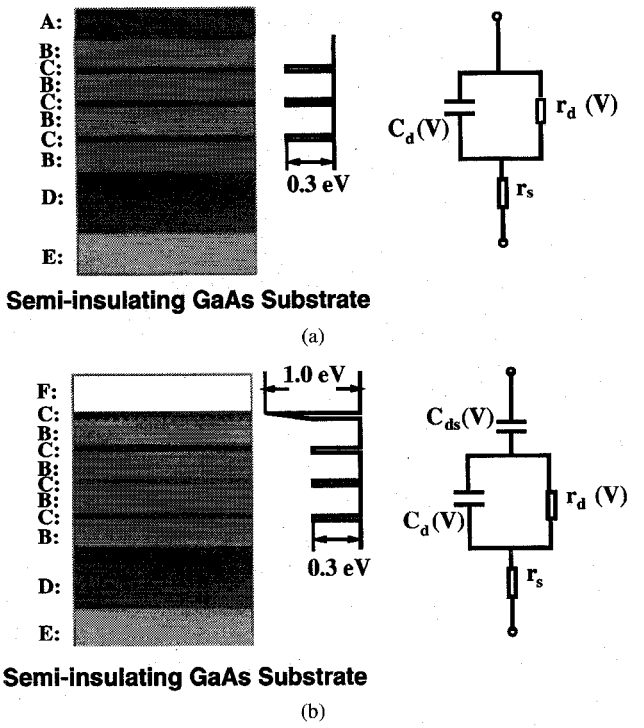

Fig. 1. Zero-bias MBE wafer profiles, band diagrams, and equivalent circuits for (a) MQBV (b) SQBV. In the above, A: 1500 Å n^+ GaAs 4×10^{18} cm^{-3}, B: 1500 Å n GaAs 1×10^{17} cm^{-3}, C: 200 Å $Al_{0.7}Ga_{0.3}As$ undoped, D: 1.0 μm GaAs 4×10^{18} cm^{-3}, E: GaAs undoped (buffer), F: 2000 Å in-situ Al, —: Si δ-doped n GaAs 3×10^{12} cm^{-2}.

is approximately ϵ/W_0, where W_0 is the zero-bias width due to the built-in voltage and is greater than 1100 Å for doping concentrations less than 10^{17} cm^{-3}. Therefore, for a barrier number less than six, the value of $C_{\max}$ for an MQBV is greater or equal to the $C_{\max}$ value of a Schottky varactor provided that the same areas are used for both devices. On the other hand, due to stacking P quantum barriers, each barrier only shares a factor of P^{-1} of the total voltage and the E-field in the depletion region (N^- layer) is significantly reduced. As a result, the MQBV breakdown voltage (specifically, the maximum voltage across P barriers) is greatly increased and the total effective depletion region of a MQBV can be significantly extended.[4] Since $C_{\min}$ per unit device area is given approximately by ϵ/L^-, the device nonlinearity, as measured by the ratio of $C_{\max}/C_{\min}$, is significantly enhanced by employing a stacking structure. Here, L^- is the total N^- layer thickness of a device. Consequently, the device cutoff frequency $f_d = (1/C_{\min} - 1/C_{\max})/2\pi r_s$ is significantly improved. Because of the advantages of the stacking structure mentioned above, one can make design tradeoffs; i.e., one can increase the device area while retaining the same capacitance value as a single barrier but reducing r_s. In addition, while the stacking structure increases the device breakdown voltage, one can also tailor the epitaxial wafer profile to maintain a large electron velocity thereby avoiding the performance degradation exhibited by standard varactors under high field conditions. Besides high f_d and high breakdown voltage, the device functions as a varactor under both forward and reverse bias due to its symmetric structure. Therefore, it naturally fits a back-to-back configuration [11], [12], simplifying the fabrication process.

The SQBV is essentially an MQBV in series with an additional Schottky barrier. Fig. 1(b) shows the MBE wafer doping profile of an SQBV together with the corresponding equivalent circuit.[5] Since the Schottky barrier is ≈ 0.5 eV higher than the $Al_{0.45}Ga_{0.55}As/GaAs$ quantum barrier, the thermal leakage current associated with the Schottky barrier is $\approx 10^8$ times smaller than that associated with the $Al_{0.45}Ga_{0.55}As/GaAs$ quantum barrier and consequently an SQBV has the same leakage current as an MQBV. The quantum barrier portion of an SQBV is the same as the MQBV. An advantage of the SQBV is that using a Schottky contact instead of an ohmic contact simplifies the fabrication procedure and still ensures a low device series resistance, r_s, of approximately 9 Ω (80 μm device area) which is comparable to that corresponding to a good ohmic contact.

In the simulations (described in Section II-B), the functional forms of $C_d(V)$ and $r_d(V)$ are obtained from curve fittings based on measurements of actual MQBV devices fabricated in our laboratory [9], [13]. Because measured data are available only up to 10 V, at which level the E-field inside the device is less than the saturation field ($E_{\max} < 2 \times 10^5$ V/cm for six barriers) but the leakage current is sufficiently large to significantly degrade device performance, the device model only includes leakage current which has a much larger effect than saturation current.[6]

Fig. 2 displays the measured C–V data together with the $C(V)$ curve used in the NLTL simulation. It should be noted that because experimental C–V data are not available for voltages in excess of 2.2 V for these initial devices, a conservative assumption that the capacitance approaches a constant value of 9.0 fF for large bias voltages is made in the simulations. The sensitivity of the predictions to this assumption was investigated. Comparison of simulations that employ this C–V curve (solid line in Fig. 2) with those employing a second C–V curve (dotted line in Fig. 2) which is identical for voltages less than 4 V, but which continues decreasing to 7.0 fF at 20 V and then becomes constant thereafter, show that the final pulse amplitude will increase by only about 5% for signal levels greater than 20 V if the second C–V curve is utilized. Here, the choice of 7.0 fF results from the summation of the theoretically calculated $C_{\min}$ (≈ 5.6 fF) and the parasitic capacitance (≈ 1.4 fF) of the device configuration. Fig. 3 shows the corresponding measured $I_d - V$ data and the $I_d(V)$ curve. The functional form of $r_d(V)$, as defined by V/I_d, is calculated from the $I(V)$ curve.

It should be noted that when the applied voltage on an MQBV, or SQBV, with six quantum barriers is greater than 10 V (about one third of its breakdown voltage), the leakage

[4]The actual physical thickness of the N^- region is only increased by half of the increment of the effective N^- region because of the back-to-back structure.

[5]Note that we employed δ-doping in the profile to obtain a larger $C_{\max}$ value for the Schottky barrier. Also the forward biased Schottky in the back-to back configuration is considered as a small resistance and is included in the device series resistance.

[6]Detailed discussion on the effect of saturation current can be found in [14].

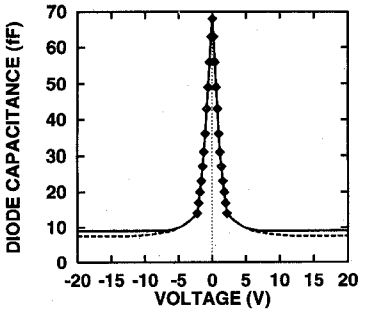

Fig. 2. Comparison of experimental C–V characteristics (◇) with the curve employed in simulations (solid line). The dotted line is utilized to study the sensitivity of the predictions to the minimum capacitance. The device (MQBV) areas is 80 μm^2.

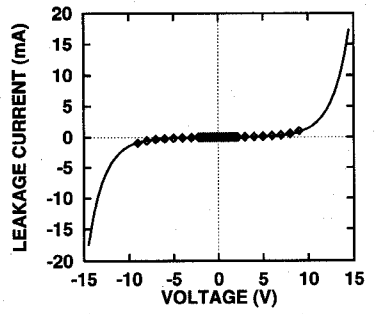

Fig. 3. Fit of experimental leakage current dependence on voltage (◇) to $I_d = 1.81 \times 10^{-2}(e^{0.45|V|} - 1)$ (mA) (dashed curve) for an MQBV device.

resistance r_d drops to a value comparable to the quantity $(\omega C_d)^{-1}$ in the frequency range at which the line operates. In fact, the value of r_d reduces exponentially as the voltage increases because the thermal leakage current through the barriers increases exponentially as the voltage increases. The decrease of r_d leads to two deleterious consequences: it degrades the line impedance match, and the significant leakage current (≈2.5 kA/cm^2 thermionic and tunneling current) generates considerable heat and loss. As a result, the performance of an NLTL is greatly degraded.

To understand the influence of the leakage current, we note that heterojunction transport theory [15] indicates that the thermionic current will be reduced by at least a factor of 500 to 1000 if the AlGaAs barrier is replaced by a superlattice structure [10] to increase the effective barrier height. We call this device a Schottky Superlattice Quantum Barrier Varactor (SSQBV). The theoretical SSQBV model, same as SQBV but with a factor of 300[7] reduction in leakage current,[8] provides us the means to study leakage current effects (see detailed discussion in Section III-B). In addition, we discuss a new lateral stacked NLTL design layout, illustrated in Fig. 4, which allows us to double or triple the signal level without increasing leakage current (see Section IV).

[7]The choice of this number is somewhat arbitrary, but serves the purpose of studying the influence of the leakage current.

[8]It should be noted, however, that our most recently fabricated SQBV devices have a leakage current reduced by a factor of $\approx 10^3$ [16] over the initial SQBV devices (perhaps due to improved fabrication). In addition, its leakage current is only a factor of five times above that of an SSQBV device.

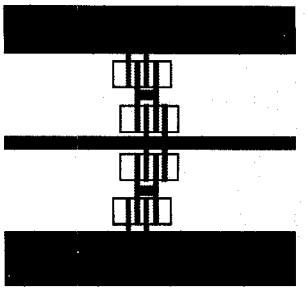

Fig. 4. New transmission line layout. The area under each solid rectangle is protected from ion implantation and includes one pair of back-to-back connected SQBV's.

B. Circuit Model for an NLTL Employing SQBV Devices

Fig. 5 shows the equivalent circuit model employed to simulate an NLTL periodically loaded with SQBV devices. Included in this model are the parasitic inductance, L_{lp}, of the fin[9] in each section, with skin effect losses in the metallized center signal line approximated by an equivalent resistance, r_l, calculated using the estimated average operating frequency of the line. The influence of the device leakage resistance, r_d, is also taken into account in this model. In addition, L and C_l are the line inductance and capacitance per section, C_d and $C_{\rm ds}$ are the device capacitances corresponding to the quantum barriers and the Schottky barrier, respectively, and r_s is the device series resistance including any contact resistance. Since the dispersion due to the periodic structure is much larger than the dispersion of the quasi-TEM mode propagating on the coplanar line [17], the contribution of the latter (≤10% of the dispersion of the periodic structure) is neglected. The parasitic capacitance of the loading device is modeled by using an experimental $C_d(V)$ curve. The parasitic capacitance of the line due to the fin line is roughly estimated, which is an order of magnitude smaller than C_l. Therefore, the parasitic capacitance of the line is neglected thereby reducing the order of equations from third to second. In this model, C_d, $C_{\rm ds}$, and r_d are functions of voltage whose forms vary according to the specific device type. In Section III-B, we discuss how to determine the values for all variables used in this model.

Applying Kirchhoff's voltage law and the charge-voltage relationship of the varactor, we obtain the following circuit equations for the nth section of the NLTL

$$I_{n+1} - I_n = -\left[\frac{\partial q_{\rm ln}}{\partial t} + \frac{\partial q_{\rm dsn}}{\partial t}\right] \tag{1}$$

$$V_n - V_{n-1} = -L_n \frac{\partial I_n}{\partial t} - I_n r_l \tag{2}$$

$$V_n - V_{\rm dn} = L_{\rm lp}\frac{\partial^2 q_{\rm dsn}}{\partial t^2} + r_s \frac{\partial q_{\rm dsn}}{\partial t} + V_{\rm dsn} \tag{3}$$

$$\frac{\partial q_{\rm dsn}}{\partial t} = \frac{\partial q_{\rm dn}}{\partial t} + \frac{V_{\rm dn}}{r_{\rm dn}(V_{\rm dn})} \tag{4}$$

$$V_{\rm dn} = f_1(q_{\rm dn}) \tag{5}$$

and

$$V_{\rm dsn} = f_2(q_{\rm dsn}). \tag{6}$$

[9]The portion inside the circle shown in Fig. 4.

In the above, $V_{\rm dn}$ and $V_{\rm dsn}$ are the voltage across C_d and $C_{\rm ds}$, respectively, $q_{\rm ln}$, $q_{\rm dn}$, and $q_{\rm dsn}$ are the charges on C_l, C_d, and $C_{\rm ds}$, f_1 and f_2 are functional forms for multi-quantum barriers and Schottky barriers, respectively. In the simulations, f_1 and f_2 are written in the following forms:

$$f_1(q_{\rm dn}) = C_0^{-1}(q_{\rm dn} + \alpha q_{\rm dn}^3) \tag{7}$$

and

$$f_2(q_{\rm dsn}) = \pm(\beta q_{\rm dsn}^2 + \gamma|q_{\rm dsn}|). \tag{8}$$

Note that in (8) the sign is always chosen to be the same as $q_{\rm dsn}$. For the 80 μm^2 SQBV, $C_0 = 7.0 \times 10^{-14}$ F, $\alpha = 7.2\times10^{25}$ C^{-2}, $\beta = 6.5\times10^{25}$ V/C^2, and $\gamma = 2.3\times10^{12}$ V/C.

In the ideal case, assuming that there are no losses or parasitics, a line capacitance much smaller than the device capacitance, and further assuming that the nonlinear device can be modeled by a single varactor with no series resistance and no leakage current, these rather complicated-looking equations reduce to two coupled equations for the current and voltage on the line. According to [18], [19], either a Toda soliton will be formed on the line if $C(V) \propto (a - V)^{-1}$ or a Korteweg de Vries (KDV) soliton will be formed if a general $C(V)$ function is expanded into polynomial form for small signal levels and under the continuum limit.[10] While these analytic results provide a physical picture of the possible waveforms propagating on the NLTL, they are very approximate. Considerable effort has been devoted toward the investigation of the properties of NLTL's using an LC-ladder type model for the transmission line [20]–[22]. However, only the simplified model is utilized. A more precise solution is necessary to describe an actual NLTL, with loss, parasitics, and a diode model more truly representing a real device. While analytical solutions for (1)–(8) are extremely difficult to obtain, numerical solutions are possible. Therefore, we developed a large signal analysis program based on the model and differential equations discussed in this section.

III. Computer Simulation

A. Effects of Device Cutoff Frequency and Symmetry of the C–V Curve on an Ideal NLTL

An understanding of how device characteristics affect the performance of an NLTL can be obtained by utilizing a simplified NLTL model which neglects skin loss, the parasitics and the leakage resistance but which retains the series resistance of the device.

The periodic loading of the nonlinear elements on an NLTL determines its low pass feature with the Bragg cutoff frequency, $f_B = \pi^{-1}[L(C_l + C_{\rm ls}]^{-1/2}$, as its upper cutoff frequency. Here, $C_{\rm ls} = \Delta Q/\Delta V$ is the large signal capacitance of the device over the voltage range ΔV. From Fourier analysis, the final pulse formed on the line, termed the line characteristic pulse, has a width inversely proportional to f_B.

[10] A soliton pulse formed on the NLTL covers more than three sections when it propagates on the line. Thus, the continuous condition, where the signal amplitude change slowly over the distance between two adjacent sections, is approximately satisfied. Therefore, n is approximately a continuous variable.

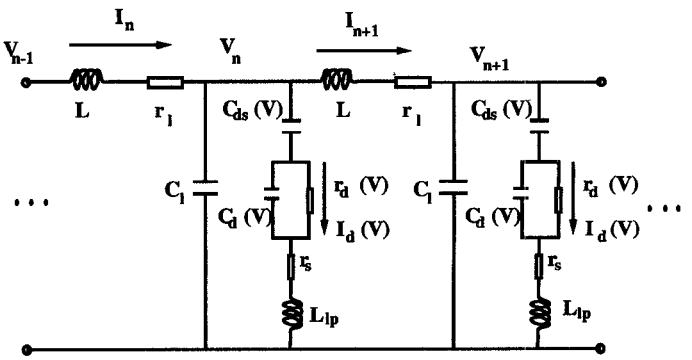

Fig. 5. Equivalent circuit diagram for an NLTL employing SQBV's.

While one can reduce the final pulse width by designing a line with high f_B, the minimum achievable pulse width, τ_s, is limited by the diode cutoff frequency, f_d. Taking both of these characteristic frequencies into account, it is found that a sharp pulse can be formed only if the ratio f_d/f_B exceeds a critical value, otherwise shock waves will result [2]. Our simulations further suggest that this critical f_d/f_B ratio which divides the pulse—NLTL from the shock-NLTL is in the range of three to six; it is a function of the device nonlinearity and is weakly dependent on line impedance.[11] This is understood by noting that f_d, defined as $f_d = \kappa/(2\pi\tau_c)$, where $\kappa = (1 - C_{\rm min}/C_{\rm max})$ is the device nonlinearity and $\tau_c = r_s C_{\rm min}$, is the minimum time constant of the device, and essentially reflects how fast and how efficiently the line can respond to and compress a signal. Because f_B is inversely proportional to the shortest pulse width which can exist on the line, the f_d/f_B ratio criterion for having a pulse—NLTL tells us that the device time constant should be sufficiently short compared with the signal width in order to respond to the signal without deformation. As mentioned before, the P barrier stacking structure of these new devices reduces $C_{\rm min}$ by a factor of P times, thereby increasing f_d significantly. As a result, the pulse duration limitation is greatly improved by utilizing these new devices on an NLTL.

The effect of alternating the sign of the input signal, which is an important feature associated with these new devices which have a symmetric $C(V)$ curve, has also been studied in the current work. It should be noted that in [19], a symmetric $C(V)$ curve has been employed to model the diode nonlinearity but only a step function has been applied to the input to observe the soliton train or oscillating tail. Here, we study a two-sided signal input to a NLTL employing two-sided devices. We define a signal having both positive and negative voltage components a two-sided signal. Otherwise, we call it a single-sided signal; i.e., a sinusoidal wave is a two sided-signal and a step-function or a Gaussian pulse is a single-sided signal. Similarly, we call a device with a symmetric $C(V)$ curve a two-sided device; otherwise, we call it a single-sided device.

A performance comparison between single-sided and two-sided devices is carried out. We first calculate the cutoff frequency of our fabricated device with area 80 μm^2; $C_{\rm max} =$

[11] However, these dependences are not exactly known at the time being and further studies are required.

70 fF; $C_{\min} = 9.0$[12] fF; $r_s = 9.6\ \Omega$.[13] From these numbers, we find $f_d = 1.6$ THz. In order to demonstrate the superior compression effects of a two-sided device, we have designed a shock wave NLTL with $f_d/f_B < 3$. Here, we assumed $f_B = 600$ GHz and a Gaussian input pulse with 20 V amplitude and 6 ps half-width incident on the NLTL loaded with ideal MQBV's (no leakage current) and observed the evolution of the waveform as it propagated down the line as shown in Fig. 6(a). We then applied a sinusoidal input wave with 20 V amplitude and 9 ps half period ($\approx$ 6 ps half-width) to the same line as shown in Fig. 6(b). Referring to Fig. 6(a), we see that a shock wave rather than sharp pulses is formed. Specifically, the line time constant is too long to respond or to break a wide pulse into the line characteristic pulse. As a result, a large tail is formed on the signal side as shown in Fig. 6(a). This is due to the fact that when $|V|$ decreases from a higher to a lower value, corresponding to $\Delta C > 0$, the transition front experiences an expansion [23]. Likewise, if $\Delta|V| > 0$ the nonlinear effect tends to compress the wave front. In Fig. 6(b), we notice that the beginning half cycle waveforms at $N = 50$ and $N = 60$ both have two peaks and are exactly the same as in Fig. 6(a). However, after the signal passes through zero voltage, starting from the second half cycle, the signal has been further broken into three peaks. The reason for this is that the strongest compression occurs at a region near zero voltage values. A sinusoidal signal periodically passes through this region and the wave is more efficiently compressed than a single-sided signal. Furthermore, a sinusoidal signal cuts off the extended tail and replaces it with a second compression region.

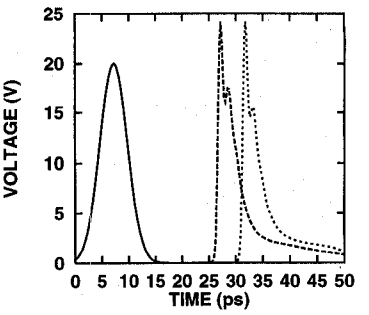

(a)

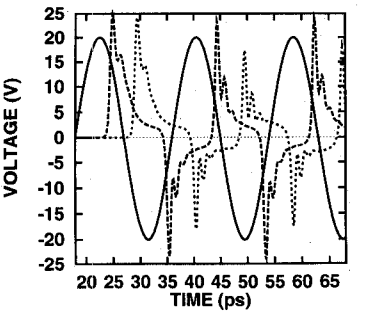

(b)

Fig. 6. (a) Evolution of the waveform when a single-sided signal is fed into an NLTL employing ideal two-sided devices with $f_B = 424$ GHz and $f_d = 1.6$ THz. (——: input; – –: $N = 50$; - - -: $N = 60$). (b) Evolution of the waveform when a two-sided signal is fed into the same line as (a) (——: input; – – $N = 50$; - - -: $N = 60$).

B. Pulse Compression Simulation of GaAs-Based NLTL's Employing SQBV's and SSQBV's

In this section, we have attempted to simulate the NLTL as realistically as possible by using the circuit model illustrated in Fig. 5 and employing parameters of devices which we have successfully fabricated. We have performed computer simulations to model NLTL's with both the SQBV and the SSQBV devices. The same device area, together with $C_{\max}$ and $C_{\min}$ values as that of the MQBV are used since they are essentially similar devices. Therefore, a diode cutoff frequency $f_d = 1.6$ THz is used in the simulations. Two f_B values, 424 GHz(Line (1)) and 212 GHz (Line (2)), are assumed by requiring the f_d/f_B ratio to produce a pulse-NLTL and final pulse widths of a few picoseconds. Once we obtained the f_d and f_B values, we followed the discussion and equations in [23], [24] to compute the line impedance, Z_l, line inductance, L, and line capacitance C_l. Possible values of Z_l ranged from 60 to 120 Ω for either coplanar wave guide or coplanar strip line [24]. From the device layout configuration, we can determine the width of the fin and the approximate expression in [23] was used to estimate the parasitic inductance, L_{lp}, of the fin. For the skin loss, the surface resistivity of gold $R_s = 9.5 \times 10^{-2}\ \Omega$ at 100 GHz was utilized (we are roughly interested in the frequency region from $\approx$ 33 to 200 GHz) to compute the power loss coefficient α_c [24]. We computed $r_l \approx 2Z_l\alpha_c$ under the approximation of $r_l \ll \omega L$ [25].[14] Utilizing these lines, we studied two limiting cases: f_B/f_{in} large and f_B/f_{in} small. A large f_B/f_{in} ratio, or a large ratio of the input pulse width to the final line characteristic pulse width, means that a wide input pulse must split into many narrow pulses and, in this case, a fast oscillating tail rather than several distinct sharp pulses is formed. As a contrast, in the second case, multiple pulses are formed. Figs. 7 and 8 show the simulation results for lines employing SSQBV's, while Figs. 9 and 10 show simulation results for the same lines employing SQBV's. First, we notice the difference between Figs. 7 and 9. In Fig. 9, there is no obvious formation of a sharp pulse. In contrast, sharp pulses are seen to start to form at section number $N = 10$ in Fig. 7 and then decrease rapidly (see the waveform at $N = 20$ in Fig. 7). Obviously, there are significantly more high frequency components in the waveform in Fig. 7 than that shown in Fig. 9. The reason is that the SQBV has much smaller leakage resistance, r_d, than the SSQBV in our simulation model. Referring to Fig. 5, we define a quality factor $Q = r_d\omega C_d$ and a barrier factor $B = r_s/Z_q$,

[12] This is a very conservative number extrapolated from capacitance measurements which range from 0 to 2.2 V.

[13] Recently, our group has perfected a new ohmic contact recipe which improved the specific contact resistance from $6 \times 10^{-6}\ \Omega \cdot \text{cm}^2$ to $3 \times 10^{-7}\ \Omega \cdot \text{cm}^2$ By using the new ohmic contact recipe, 9.6 Ω series resistance is easily achieved. We also notice that our present device configuration can be further improved to reduce the loss.

[14] Note the first line has $f_B \approx 400$ GHz which exceeds the frequency range we used to estimate R_s. The average R_s of this line is a factor of $2^{1/2}$ larger than the value used in the simulation since $R_s \propto f^{1/2}$. Therefore, the power loss coefficient will increase by a factor of $2^{1/2}$ correspondingly and the voltage level will be 4% lower than the value presented here after the wave propagates 10 sections on the first line.

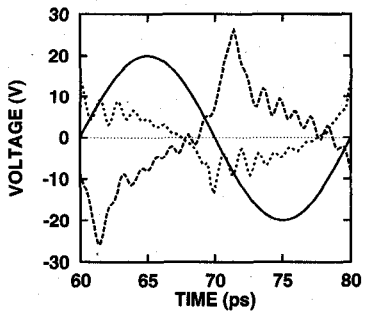

Fig. 7. Waveforms on Line (1) with an SSQBV as the nonlinear element. $f_B = 424$ GHz. $T_{\text{input}} = 20$ ps. (——: input; – –: $N = 10$; - - -: $N = 20$).

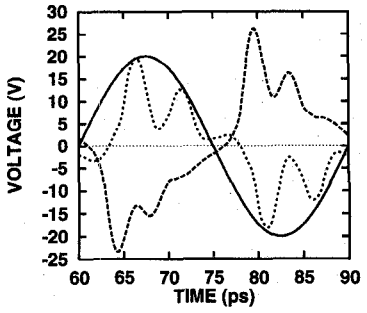

Fig. 8. Waveforms on Line (2) with an SSQBV as the nonlinear element. $f_B = 212$ GHz. $T_{\text{input}} = 30$ ps. (——: input; – –: $N = 10$; - - -: $N = 20$).

where Z_q is the total quantum barrier impedance (shunt C_d and r_d) and r_s is the series resistance. The larger the value of Q and the smaller the value of B, the better performance a quantum barrier device will have. Both the SQBV and SSQBV devices have comparable values of r_s while the SSQBV has a much larger value of r_d than the SQBV. Therefore, the SSQBV has a larger Q value and a smaller B value as compared with the SQBV. As a result, the SSQBV exhibits enhanced performance which in turn means that additional higher harmonics can be generated and propagated. Second, we see that 4 ps duration pulses are formed at section $N = 20$ with amplitudes of ≈ 16 V and ≈ 10 V on Line (2) employing SSQBV's and SQBV's, respectively. If we compare the evolved waveforms of an actual line with that of an ideal line (see Fig. 6(b)), we observe that the signal level drops to ≈ 16 V at $N = 20$ on a real line while it happens at $N = 60$ on an ideal line. The dramatically reduced amplitude, compared with that of the ideal case, is due partially to losses associated with r_l but mainly to the leakage current. Third, with $f_B = 424$ GHz, Line (1) should generate 1.5 ps duration pulses. However, sharp pulses are not distinctly formed on Line (1) employing either the SQBV or the SSQBV devices due to the large losses. Using semi-quantitative arguments, we can demonstrate that narrower pulses experience more rapid loss. According to [18], the sharp pulses formed on NLTL's are solitons with amplitudes proportional to Ω^2 and widths inversely proportional to $(\Omega + \Omega^2/6)$, where Ω is a variable associating soliton amplitude with soliton width in the analytic soliton expression. Assume, for simplicity, that the input pulse is only wide enough to form a single sharp pulse and that the total equivalent loss resistance is r_t. Therefore, the average energy loss per cycle is:

$$P_{\text{loss}} = \frac{\langle V_{\text{amplitude}} \rangle^2}{r_t} T_{\text{pulse width}} \propto \frac{\Omega^3}{r_t(t + \frac{\Omega}{6})}. \quad (9)$$

For a very narrow soliton which has a larger Ω value, this loss is actually proportional to Ω^2. Therefore, the loss will increase as the wave is compressed and the line loss should therefore be particularly small in order to generate very narrow solitons.

C. Harmonic Generation Simulation of InP-Based NLTL's Employing SQBV's

One difficulty concerning conventional varactor multipliers is that it is difficult to obtain high conversion efficiency

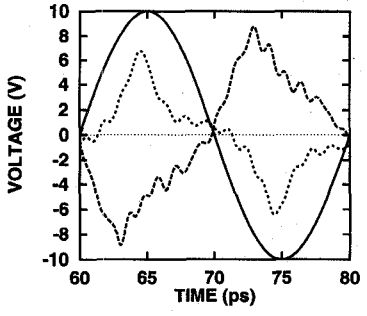

Fig. 9. Waveforms on Line (1) with an SQBV as the nonlinear element. $f_B = 424$ GHz. $T_{\text{input}} = 20$ ps. (——: input; – –: $N = 10$; - - -: $N = 20$).

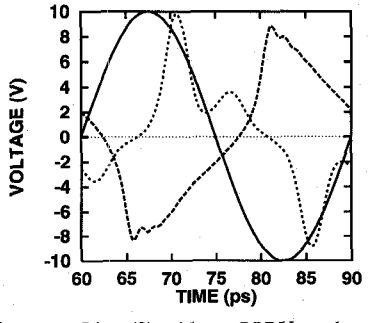

Fig. 10. Waveforms on Line (2) with an SQBV as the nonlinear element. $f_B = 212$ GHz. $T_{\text{input}} = 30$ ps. (——: input; – –: $N = 10$; - - -: $N = 20$).

over a broad bandwidth because their reactive input and output impedances can only be matched efficiently at certain frequencies. In contrast, by using NLTL's all harmonics lower than f_B can be effectively coupled out. With a proper design, a comb-like signal can be generated from an NLTL.

A signal formed on an NLTL comprised of two-sided devices is symmetric with respect to positive and negative voltages. As a result, the even harmonics are canceled while the odd harmonics are doubled when compared to a single-sided NLTL. For harmonic generation applications, one is primarily concerned with the harmonic conversion efficiency, η. In general, the larger the f_d value, the higher η is. There are two reasons for this. First, the f_d/f_B ratio requirement for having a pulse-NLTL has to be met in order to obtain maximum pulse compression and harmonic generation. Second, a large f_d value means small loss which is necessary for a high η value. Because, in most cases, f_d is limited by factors difficult to improve, we do not take f_d as a parameter

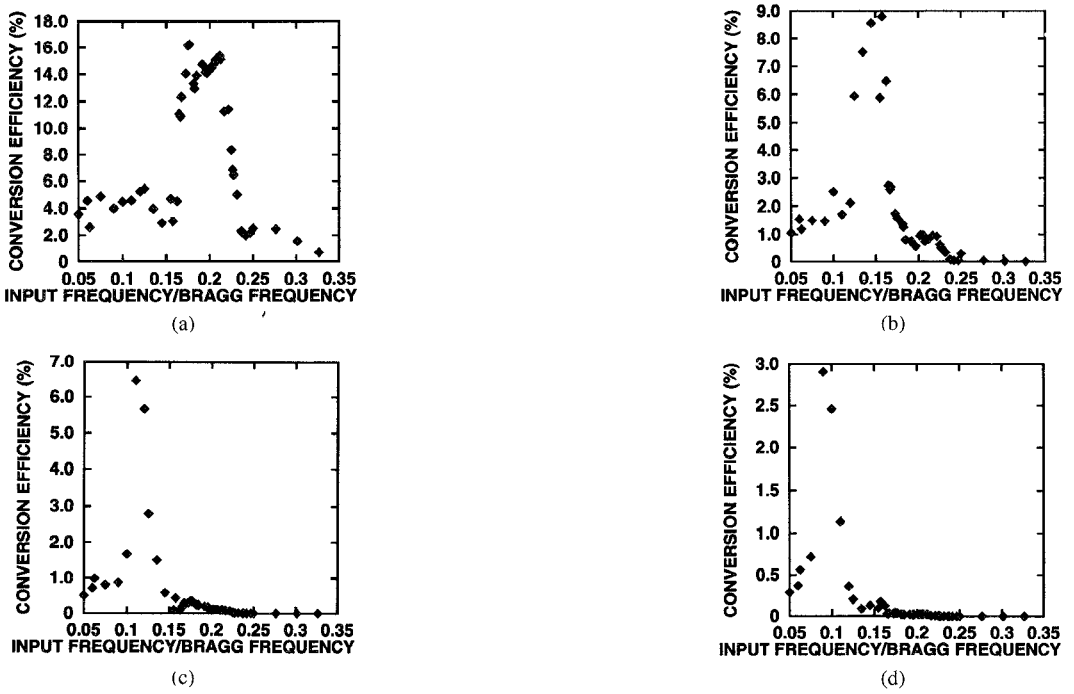

Fig. 11. Optimum harmonic conversion efficiencies, ν, as a function of the input frequency normalized to the Bragg frequency for the line with InP-based SQBV's and $Z_l = 120\ \Omega$. (a) Third harmonic. (b) Fifth harmonic. (c) Seventh harmonic. (d) Ninth harmonic.

which can be easily changed. In contrast, f_B, Z_l etc. are easily changed by varying the configuration and size of the line. Therefore, in the following, we demonstrate how to design line parameters to achieve maximum η for a given harmonic assuming that f_d is fixed. In order to achieve a high value of f_d, the design utilizes InP based SQBV's. Because InP based material has a higher electron mobility than GaAs material, a lower r_s value is expected. Therefore, in this simulation, the device parameters are: $C_{\max} = 55.8$ fF, $C_{\min} = 11.2$ fF and $r_s = 3.0\ \Omega$ which result in $f_d = 3.79$ THz. Again, these parameters are consistent with our array fabrication experience. To avoid power conversion into harmonics higher than desired, $f_B = 200$ GHz is chosen. The line impedance (without device loading) is 120 Ω. By scanning the frequency of the input sine-wave, we are able to study conversion efficiencies for the first four nonzero harmonics (third, fifth, seventh, and ninth) for various values of f_{in}/f_B. The results of this study are plotted in Fig. 11. The fluctuations in the predicted conversion efficiencies appear to result from the standing waves on the NLTL due to mismatched impedances.[15] This interpretation has been verified by letting the line length become extremely long to prevent reflections coming back to the location where the samples are taken. As a result, the curves were seen to become smoother.

A better understanding of the numerical results can be obtained by a simple analytic study. To a first order approximation, we utilize the following function to approximate the waveform shown in Fig. 7 which corresponds to the case with a small f_{in}/f_B ratio:

$$V(t) = \begin{cases} \cos(\pi t/T)(1-\cos\omega t), & t < T/2 \\ -\cos\pi(t/T-1/2)\{1-\cos[\omega(t-T/2)]\}, & T/2 < t < T \end{cases} \tag{10}$$

In the above, T is the input signal period, $\omega = 2\pi\theta_0/\gamma T$, $\gamma = f_{\text{in}}/f_B$, and $\theta_0 = 0.82$ reflects the weak dependence of the signal amplitude and is related to the nonlinearity of our device. Alternatively, we can employ a Gaussian function to approximate waveforms similar to those shown in Fig. 8 which correspond to the case with a large f_{in}/f_B ratio. The Fourier transform is applied to these functions from which the conversion efficiency for each harmonic follows. The maximum conversion efficiency occurs around $f_{\text{in}}/f_B = \theta_0/n$, where $n = 3, 5\cdots$ is the odd harmonic number. The analytic results are consistent with the numerical study. The only difference is that the analytic efficiency, η_0, is larger than the numerical efficiency, η_i. This is because η_0 is referred to the output signal and η_i is referred to the input signal. Since there are losses along the NLTL, it is inevitable that $\eta_i < \eta_0$.

Regardless of the fluctuations in the numerical results, several features are evident. First, the optimum ratio of f_{in}/f_B, at which the maximum conversion efficiency is obtained, differs for different harmonics and shifts to a smaller value for a higher harmonic. This occurs because a smaller value of f_{in}/f_B means a higher compression ratio of the input and output pulse widths which in turn means that more higher harmonic components are involved in the compression process. Second, the optimum efficiency decreases for a higher harmonic. This reflects the low-pass nature of the periodic NLTL as well as conservation of energy. Since any frequency lower than the cutoff frequency, f_B, shares the energy, a

[15] The line impedance varies from 36 to 69 Ω as the signal amplitude swings from low to high. Because the line is terminated by a 50 Ω load, impedance mismatches resulted.

TABLE I
UPPER FREQUENCY LIMIT FOR VARIOUS LATERAL STACKING NUMBERS, ($M \leq 4$)

	$f_B(GHz)$	$S(\mu m^2)$	W_d/D	C_p/C_{min}	$\tau_{s0}(ps)$	$\tau_s(ps)$
M=1	1000	2x2x5xM²	0.35	0.5	1.0	1.6
M=2	120	2x4x21xM²	0.19	0.45	8.3	11.8
M=3	80	2x6x21xM²	0.28	0.34	12.5	16.8
M=4	50	2x8x25xM²	0.27	0.29	20.0	25.8

lower ratio of f_{in}/f_B, or a higher cutoff frequency, means generation of more harmonics but also means the distribution of the energy over all these harmonics which result in a lower conversion efficiency for the higher harmonic. Third, by adjusting the f_{in}/f_B value, we can either balance η values for all required harmonics to obtain broadband harmonic generation, or obtain the highest η for a particular harmonic.

IV. LATERAL STACKING CONFIGURATION

The simulation results in Section III-B clearly show that the application of an SQBV is greatly limited by its large leakage current at voltage levels higher than 10 V which is only one-third of its breakdown voltage. Thus, the leakage current must be reduced. While increasing the effective barrier height significantly improved the signal level as shown in Section III-B, we can further extend the diode voltage range by stacking devices laterally along the coplanar line crossing strip as shown in Fig. 4. Note that this design configuration only fits two-side devices.

Because there is a fin interconnecting the transmission line and the device in the NLTL layout, the new design configuration adds only a little structural detail to the fin. These structural details do not significantly affect the fin parasitic inductance but will add more parasitic capacitance. Specifically, for frequencies lower than 120 GHz and line impedances less than 90 Ω, the parasitic capacitances are much smaller than the line capacitance. Therefore, the new layout design will not change the line performance except to double or triple the voltage handling capability of the line depending upon the minimum pulse duration requirements. This improved voltage handling capability together with moderately fast pulse output ($\approx$ 8.0 ps) is of importance in many applications such as fusion plasma reflectometric diagnostics [26]. According to coplanar line design rules (discussed in Section III-B), the space between two sections is $D = A/f_B$, the gap between the center line and the ground plane is $b = G/f_B$ and the required device area is $S = H/f_B$. Here, A and G are functions of the line impedance, Z_l, and the line large signal impedance, Z_{ls}, while H is a function of Z_l, Z_{ls} and the device large signal capacitance per unit area, C_{ls}. For $Z_l = 90\ \Omega$, $Z_{\text{ls}} = 50\ \Omega$ and $C_{\text{ls}} = 0.22$ fF/μm^2, $A = 2.0 \times 10^{13}$ μm/s, $G = 6.2 \times 10^{12}$ μm/s and $H = 2.0 \times 10^{13}$ μm^2/s. Note that C_{ls} is computed based upon experimentally measured C–V data. It is readily seen that as f_B increases there is not sufficient space to fit the lateral stacking structure without introducing large parasitics and violating the quasi-TEM mode condition. In Table I, we have listed the results of a study on the upper frequency limit as a function of the lateral stacking number ($M \leq 4$).

In Table I, f_B is the Bragg cutoff frequency, S is the total device area in both coplanar wave guide (CPW) gaps, W_d is the total device finger width, C_p is the parasitic capacitance, τ_{s0} is the pulse width without considering the effect of C_p and τ_s is the pulse width including the effect of C_p. In the third column, the first number is the number of gaps in the CPW, the second number is the width of each finger, the third number is the length of each finger and the M^2 factor results from the M times lateral device stacking and the fact that since they are stacked in series each device area has to be increased by a factor of M. The C_p value is calculated as an interdigitated capacitor [27] with a 3-μm gap between fingers. From the table, the trade off is obvious. While we increase the lateral stacking number to increase the signal power, the corresponding minimum pulse duration increases as well. To illustrate the effect of the new design layout, we designed 40-section tapered NLTL's employing SQBV's with the first N sections applying the lateral stack configuration. A coplanar strip line arrangement is chosen with a line impedance of 100 Ω to reduce line losses at high impedance. The device parameters and line design rules are exactly the same as those described before. However, the value of f_B starts at 14 GHz and increases geometrically for every two sections to 139 GHz. The input signal is a Gaussian pulse with a half amplitude width of 90 ps and an amplitude of 10 V. In Fig. 12, we plot the final peak signal value versus the number of sections, N, which employ the lateral stacked structure. We see that the signal peak is improved from 9.7 V to 19.6 V if all the sections employ the lateral stacked structure. Here, it is helpful to note that, in the stacked structure, each device only shares part of the signal voltage which corresponds to a much smaller leakage current since the leakage current increases exponentially with voltage. Consequently, the peak signal level experiences significantly less dissipation and the line is allowed to take full advantage of the improved breakdown voltage for the SQBV. The slowly rising peak level for $N \leq 30$ and the dramatic fast rising peak level for $N > 36$ clearly indicate the severe effect of the leakage current. As long as there is one section without the stacked structure, the signal level drops significantly due to the generation of a large leakage current at that section which results in a large dissipation and a large reduction of r_d as well as Z_q. In general, the signal level on NLTL's that utilize the lateral stacked structure will be doubled or tripled if the final required pulse durations exceed 8.3 or 12.5 ps and will still be significantly improved for pulse durations between 2.5 and 8.3 ps by combining the lateral stacking structure with the tapered line design.

V. CONCLUSION

From these studies, we conclude that an impulse with 2.5 to 4 ps pulse width, 16 to 19.6 V pulse peak can be achieved on an NLTL employing either SSQBV's or SQBV's with the new lateral stack design and 2 μm design rules. Since the simulations are based on experimentally measured C–V curves and r_s values from the first preliminary fabrications of these devices, we expect that the predicted performance is quite conservative. For example, the device configuration can be improved to reduce device loss thereby increasing the device

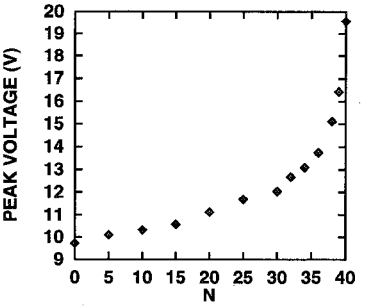

Fig. 12. The peak signal value versus the number of sections, N, which employ the lateral stacked structure.

cutoff frequency. In fact, measurements from our recently fabricated devices indicate that the leakage current can be reduced by improving the fabrication process. In general, by employing these new devices the final pulse width is reduced (the stacking structure results in a reduction of $C_{\min}$ and hence the pulse width), the signal amplitude is increased and the number of sections needed to compress the input pulse into the final pulse is reduced and NLTL's with these device can operate with both polarity signals. Harmonic generation on NLTL's utilizing these new devices is studied as well. Because of the increased breakdown voltage which reduces the loss and two-sided wave compression feature of these new devices, a higher conversion efficiency is expected.

ACKNOWLEDGMENT

The authors thank Profs. Brian Kolner and D. S. Pan for critical reviews of the manuscript as well as numerous technical discussions.

REFERENCES

[1] M. J. W. Rodwell, D. M. Bloom, and B. A. Auld, "Nonlinear transmission line for picosecond pulse compression and broadband phase modulation," *Electron. Lett.*, vol. 23, pp. 109–110, 1987.

[2] M. J. W. Rodwell, M. Kamegawa, R. Yu, M. Case, E. Carman, and K. S. Giboney, "GaAs nonlinear transmission lines for picosecond pulse generation and millimeter-wave sampling," *IEEE Trans. Microwave Theory Tech.*, vol. 39, pp. 1194–1203, 1991.

[3] M. S. Shakouri, A. Black, B. A. Auld, and D. M. Bloom, "500 GHz GaAs MMIC sampling wafer probe," *Electron. Lett.*, vol. 29, pp. 557–558, 1993.

[4] R. A. Marsland, M. S. Shakouri, and D. M. Bloom, "Millimeter-wave second harmonic generation on a nonlinear transmission line," *Electron. Lett.*, vol. 26, pp. 1235–1237, 1990.

[5] E. Carman, K. S. Giboney, M. Case, M. Kamegawa, R. Yu, K. Abe, M. J. W. Rodwell, and J. Franklin, "28–39 GHz distributed harmonic generation on a soliton nonlinear transmission line," *IEEE Microwave and Guided Wave Lett.*, vol. 1, pp. 28–30, 1991.

[6] E. Carman, M. Case, M. Kamegawa, R. Yu, and M. J. Rodwell, "V-Band and W-band broadband, monolithic distributed frequency multipliers," presented at *IEEE Microwave Theory Tech. Soc. Int. Microwave Symp.*, Albuquerque, NM, June 1–5, 1992.

[7] M. Case, E. Carman, R. Yu, and M. J. W. Rodwell, "Picosecond duration, large-amplitude impulse generation using electrical soliton effects," *Appl. Phys. Lett.*, vol. 60, pp. 3019–3021, 1992.

[8] C. J. Madden, R. A. Marsland, M. J. W. Rodwell, and D. M. Bloom, "Hyperabrupt-doped GaAs nonlinear transmission line for picosecond shockwave generation," *Appl. Phys. Lett.*, vol. 54, pp. 1019–1021, 1989.

[9] H.-X. L. King, L. B. Sjogren, N. C. Luhmann, Jr., and D. B. Rutledge, "New concepts for high frequency and high power frequency multipliers and their impact on quasi-optical monolithic array design," *Int. J. Infrared and Millimeter Wave*, vol. 13, pp. 251–265, 1992.

[10] C. Raman, J. P. Sun, W. L. Chen, G. Munns, J. East, and G. Haddad, "Superlattice barrier varactors," in *Proc. Third Int. Symp. Space Terahertz Tech. Symp.*, Ann Arbor, MI, 1992, pp. 146–157.

[11] U. Lieneweg, B. R. Hancock, and J. Maserjian, "Barrier-intrinsic-N$^+$ (BIN) diodes for near-millimeter wave generation," in *Proc. 1987 IEEE 12th Int. Conf. Infrared and Millimeter Waves*, 1987, pp. 6–7.

[12] H.-X. L. Liu, X.-H. Qin, L. B. Sjogren, W. Wu, E. Chung, C. W. Domier, and N. C. Luhmann, Jr., "Monolithic millimeter-wave diode grid frequency multiplier arrays," in *Proc. 3rd Int. Symp. Space Terahertz Technol.*, Ann Arbor, MI, 1992, pp. 595–599.

[13] H.-X. L. Liu, L. B. Sjogren, C. W. Domier, N. C. Luhmann, Jr., D. L. Sivco, and A. Y. Cho, "Monolithic quasi-optical frequency tripler array with 5 W output power at 99 GHz," *IEEE Electron Dev. Lett.*, vol. 14, pp. 329–331, 1993.

[14] E. L. Kollberg, T. J. Tolmunen, M. A. Frerking, and J. R. East, "Current saturation in submillimeter wave varactors," *IEEE Trans. Microwave Theory Tech.*, vol. 40, pp. 831–838, 1992.

[15] F. Capasso and G. Margaritondo, *Heterojunction Band Discontinuities*. Amsterdam, The Netherlands: North-Holland, 1987, pp. 451–487.

[16] Weimin Zhang, X.-H. Qin, Y. Liao, R. W. Grek, R. P. Hsia, F. Jiang, Y. Li, C. W. Domier, and N. C. Luhmann, Jr., "Monolithic nonlinear transmission lines using multi-barrier devices," presented at *5th Int. Symp. Space Terahertz Technol.*, May 10–12, 1994, Ann Arbor, MI.

[17] M. Y. Frankel, S. Gupta, J. A. Valdmanis, and G. A. Mourou, "Terahertz attenuation and dispersion characteristics of coplanar transmission lines," *IEEE Trans. Microwave Theory Tech.*, vol. 39, pp. 910–916, 1991.

[18] H. Nagashima and Y. Amagishi, "Experiment on the Toda lattice using nonlinear transmission lines," *J. Phys. Soc. Jap.*, vol. 45, pp. 680–688, 1978.

[19] H. Ikezi, S. S., Wojtowicz, R. E., Waltz, J. S. deGrassie, and D. R. Baker, "High-power soliton generation at microwave frequencies," *J. Appl. Phys.*, vol. 64, pp. 3277–3281, 1988.

[20] T. Tsuboi and F. M. Toyama, "Computer experiments on solitons in a nonlinear transmission line, I. Formation of stable solitons," *Phys. Rev.*, vol. A 44, p. 2686, 1991.

[21] T. Tsuboi, "Formation process of solitons in a nonlinear transmission line: Experimental study," *Phys. Rev.*, vol. A 41, p. 4534, 1990.

[22] M. Toda, "Wave propagation in anharmonic lattices," *J. Phys. Soc. Japan.*, vol. 23, pp. 501–506, 1967.

[23] M. J. W. Rodwell, "Picosecond electrical wavefront generation and picosecond optoelectronic instrumentation," Ph. D. dissertation, Stanford University, 1988.

[24] K. C. Gupta, R. Garg, and I. J. Bahl, *Microstrip Lines and Slotlines*. Dedham, MA: Artech House, 1979.

[25] David M. Pozar, *Microwave Engineering*. Reading, MA: Addison Wesley, 1990.

[26] N. C. Luhmann, Jr., S. Baang, D. L. Brower, S. Burns, A. Chou, E. J. Doyle, J. Howard, Y. Jiang, W. A. Peebles, R. Philipona, C. Rettig, and T. L. Rhodes, "Millimeter and submillimeter wave diagnostics for contemporary fusion experiments," in *ISPP-9*, Societá Italiana di Fisica, Varenna, Italy, 1991, pp. 135–178

[27] P. H. Ladbrooke, *MMIC Design: GaAs FET's and HEMT's*. Boston, MA: Artech House, 1989, p. 41.

Hui Shi received the B.S. degree in physics from Fudan University, Shanghai, China, in 1984, and the M.S. degree in physics from California State University, Los Angeles, in 1990. Currently she is working toward the Ph.D. degree in physics at University of California, Los Angeles.

Her research involves semiconductor device design, large-signal modeling, fabrication of monolithic microwave and millimeter-wave integrated circuits, and the circuit measurements.

W.-M. Zhang, photograph and biography not available at the time of publication.

C. W. Domier, photograph and biography not available at the time of publication.

N. C. Luhmann, Jr., photograph and biography not available at the time of publication.

L. B. Sjogren, photograph and biography not available at the time of publication.

H.-X. L. Liu, photograph and biography not available at the time of publication.